environments

Article

Optimizing Vineyard Pruning Biochars for Nutrient Adsorption: Toward Sustainable Fertilizer Applications

Olena Dorosh [1], Andreia F. Peixoto [2], Cristina Delerue-Matos [1], Paula M. L. Castro [3] and Manuela M. Moreira [1,*]

[1] REQUIMTE/LAQV, Instituto Superior de Engenharia do Porto, Instituto Politécnico do Porto, Rua Dr. António Bernardino de Almeida, 431, 4249-015 Porto, Portugal; anelo@isep.ipp.pt (O.D.); cmm@isep.ipp.pt (C.D.-M.)
[2] REQUIMTE/LAQV, Department, de Química e Bioquímica, Faculdade de Ciências, Universidade do Porto, Rua do Campo Alegre s/n, 4169-007 Porto, Portugal; andreia.peixoto@fc.up.pt
[3] CBQF—Centro de Biotecnologia e Química Fina—Laboratório Associado, Escola Superior de Biotecnologia, Universidade Católica Portuguesa, Rua de Diogo Botelho, 1327, 4169-005 Porto, Portugal; plcastro@ucp.pt
* Correspondence: mmdsm@isep.ipp.pt; Tel.: +351-228340500

Abstract

Agricultural residues, such as vineyard prunings, are abundant yet underutilized resources with potential for conversion into value-added products. In this study, vineyard prunings were investigated for the first time as feedstock for nutrient-enriched biochars intended for use as enhanced efficiency fertilizers (EEFs). Four biochars were produced using distinct physical (industrial-scale pyrolysis, CO_2-assisted pyrolysis) and chemical ($MgCl_2$, $AlCl_3$ pretreatment) procedures. Their adsorption capacities for nitrogen (N), phosphorus (P), and potassium (K) were evaluated across a wide pH range (2–13). Optimization studies, including dosage, kinetics, and isotherms, revealed maximum Langmuir adsorption capacities of 10.4 mg N g^{-1} and 12.7 mg P g^{-1}, which were comparable to or higher than other low-cost agricultural biochars, confirming the competitive performance of vineyard pruning-derived biochars. Beyond adsorption efficiency, these biochars provide additional benefits by valorizing a widely available viticulture residue, reducing open-field disposal and burning, and generating low-cost fertilizers that may reduce nutrient leaching and improve soil health. This work introduces a novel circular pathway linking vineyard waste management to sustainable nutrient delivery, integrating agricultural byproduct utilization with environmental remediation strategies.

Keywords: vineyard pruning; adsorption; phosphorus; nitrogen; biochar; enhanced efficiency fertilizers

Academic Editors: Gabriel Gascó Guerrero, Ana Méndez and Jorge Paz-Ferreiro

Received: 7 November 2025
Revised: 10 December 2025
Accepted: 12 December 2025
Published: 15 December 2025

Citation: Dorosh, O.; Peixoto, A.F.; Delerue-Matos, C.; Castro, P.M.L.; Moreira, M.M. Optimizing Vineyard Pruning Biochars for Nutrient Adsorption: Toward Sustainable Fertilizer Applications. *Environments* **2025**, *12*, 491. https://doi.org/10.3390/environments12120491

1. Introduction

Biochar, a carbon-rich porous material produced through the thermal conversion of biomass under oxygen-limited conditions, has attracted increasing attention for agricultural and environmental applications [1,2]. Its physicochemical properties—surface area, porosity, and functional groups—depend strongly on feedstock and pyrolysis conditions [2,3]. These attributes give biochar a high cation exchange capacity and adsorption potential, enabling applications in environmental remediation, catalysis, electrochemical devices, and as soil amendments or carriers in agricultural formulations [4–8].

In agriculture, biochar-based enhanced efficiency fertilizers (EEFs) are emerging as sustainable alternatives to conventional fertilizers [9–13]. Although conventional fertilizers

were initially developed to meet the food demands of a growing global population and have significantly enhanced crop yields and soil fertility, their widespread use has also caused environmental degradation and increased economic costs [11,12]. Nitrogen (N), phosphorus (P), and potassium (K) are essential macronutrients for plant growth, with global demand reaching 185.06 million tons in 2016 [12]. However, these fertilizers exhibit low nutrient use efficiency: between 40–70% of N, 80–90% of P, and 50–70% of K can be lost through volatilization, leaching or runoff [12]. These inefficiencies contribute to atmospheric (NH_3, N_2O) and water (NO_3^-) pollution in the case of N, and to eutrophication in the case of P, a non-renewable resource [12,14]. Incorporating nutrients into biochar matrices offers a promising solution, allowing gradual nutrient release aligned with plant uptake while minimizing environmental losses [11]. Additionally, biochar amendments can improve soil organic matter, water retention, and porosity [2,8,15].

Despite these advantages, pristine biochars typically have low nutrient content and limited adsorption efficiency, requiring targeted modifications to enhance their performance [2]. Physical and chemical treatments can improve microporosity, increase surface functional groups, and alter the pH at the point of zero charge (pHPZC), which is particularly relevant for enhancing the adsorption of anionic nutrients such as nitrate (NO^{3-}) and phosphate (H_2PO_4, HPO_4^{2-}, PO_4^{3-}) [1,2,6,8]. The choice of modification strategy, including feedstock type, pyrolysis conditions, and chemical additives, strongly determines the resulting adsorption capacity [2].

Grape cultivation, particularly for winemaking, represents a major agricultural sector in Europe, with France, Spain, Italy and Portugal as leading producers [16]. In 2022, the continent accounted for 3.3 million hectares of vineyards [17]. Vineyard management requires annual pruning to maintain yield and plant health, generating approximately 1.75 tons of lignocellulosic residues per hectare per year [18]. While these prunings are often left in the soil, incorporated, or burned, their low density makes transport and disposal costly, highlighting the need for local valorization strategies [19]. Converting vineyard prunings into biochar provides a circular solution that both reduces waste and generates value-added products. Previous studies have explored vineyard prunings as feedstock for biochar and activated carbon production [20–24]. However, to date, little attention has been given to their nutrient adsorption and enrichment potential for fertilizer applications.

This study addresses this gap by transforming vineyard prunings into nutrient-enriched biochars through distinct physical (CO_2-assisted pyrolysis, industrial-scale pyrolysis) and chemical ($MgCl_2$, $AlCl_3$ pretreatment) modification strategies. Four biochars were produced and systematically evaluated for their adsorption capacities toward N, P, and K. To our knowledge, this is the first work to: (i) directly compare industrial-scale and laboratory-scale pyrolysis systems for vineyard prunings in the context of nutrient adsorption, (ii) apply Mg^{2+} and Al^{3+} pretreatments to vineyard pruning-derived biochars for targeted nutrient capture, and (iii) benchmark their adsorption capacities against relevant studies in the literature. By linking an abundant regional residue with the development of EEFs, this work proposes a novel and sustainable valorization pathway for vineyard waste while advancing strategies for improved soil fertility management.

2. Materials and Methods

2.1. Reagents

For the biochar's chemical activations, aluminium chloride ($AlCl_3$, 99.5%) was acquired from José M. Vaz Pereira, Lda (Lisbon, Portugal) and magnesium chloride hexahydrate ($MgCl_2.6H_2O$, 99.0%) from VWR chemicals (Leuven, Belgium). For the pH adjustments, sodium hydroxide (NaOH, for analysis) was purchased from Labchem (Santo Antão do Tojal, Portugal) and hydrochloric acid (HCl, ≥37.0%) from Honeywell Fluka (Seelze,

Austria). For the adsorption studies, sodium nitrate ($NaNO_3$, ≥99.5%) was acquired from Riedel-de-Haën (Hannover, Germany), potassium phosphate monobasic (KH_2PO_4, ≥99.0%) from Sigma (St. Louis, Missouri, United States of America), and potassium chloride (KCl, 99.5%) from Honeywell Fluka (Hannover, Germany). Potassium bromine (KBr, ≥99.0%) for the Fourier-transform infrared spectroscopy (FTIR) analysis was obtained from Riedel-de-Haën (Hannover, Germany). For the potassium quantification, antimony potassium tartrate ($K_2Sb_2(C_4H_2O_6)_2$, for analysis) from Carlo Erba (Barcelona, Spain), ammonium molybdate tetrahydrate ($(NH_4)6Mo_7O_{24}.4H_2O$, ≥99.5%) from Honeywell Fluka (Bengaluru, India), ascorbic acid (99%) from Riedel-de-Haën (Shenyang, China) and sulfuric acid (H_2SO_4, 95.0–97.0%) from Honeywell Fluka (Hannover, Germany) were purchased.

2.2. Biochar Preparation

Vineyard prunings from the Touriga Nacional variety, kindly provided by Sogrape, were used as raw material to produce four distinct biochars, as illustrated in Figure 1. The vineyard prunings were randomly collected after harvest season and air-dried for four weeks prior to biochar production. During drying, the material was manually mixed at regular intervals to ensure uniform exposure to air and consistent moisture loss across all canes. The first biochar was produced in industrial ovens at the Ibero Massa Florestal company (BIMF), following conditions previously described by Fernandes et al. [5]. The process consisted of 8 h of heating, at a rate of 50 °C/h, 14 h of holding at 400 °C, and cooling to room temperature. Pyrolysis was performed under limited air availability with only residual oxygen present after sealing the oven. This route was selected to represent large-scale industrial conditions, as production cost-effectiveness and scalability are critical for future applications. The second biochar was produced in a tubular furnace under a continuous CO_2 flow (BCO_2). Prior to pyrolysis, vineyard prunings were milled using a laboratory mill (Retsch ZM200, Haan, Germany) and sieved to a particle size between 1 and 2 mm. Pyrolysis was performed under a CO_2 flow of 100 mL/min, with a heating rate of 20 °C/min, a holding period of 1 h at 400 °C, and subsequent cooling to room temperature. The use of CO_2 as a carrier gas has been reported to promote activation and partial oxidation reactions that can increase porosity and surface area, thereby enhancing adsorption properties [25,26]. This approach was included to assess whether gas-assisted pyrolysis could provide enhanced nutrient retention relative to the other methods tested.

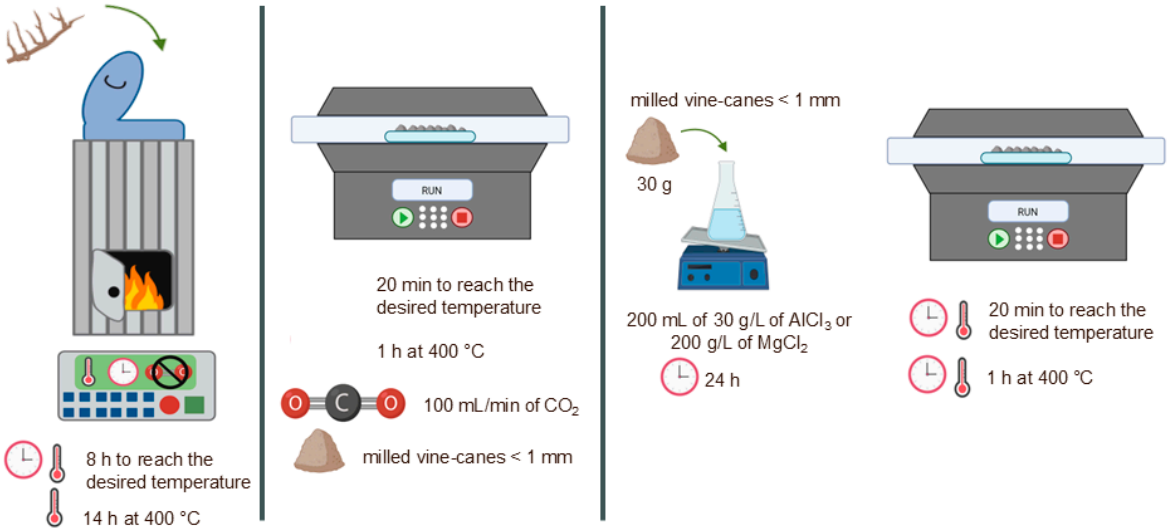

Figure 1. Schematic illustration of the processes employed to obtain the four biochars investigated in this work: BIMF (biochar prepared at Ibero Massa Florestal company), BCO_2 (biochar prepared with a flux of CO_2), $BAlCl_3$ (biochar pretreated with $AlCl_3$), $BMgCl_2$ (biochar pretreated with $MgCl_2$).

The other two biochars were produced via chemical pre-treatment. For this, 30 g of milled vineyard prunings were immersed in 200 mL of $AlCl_3$ (30 g/L) or $MgCl_2$ (200 g/L) solutions prepared with deionized water. The mixtures were stirred for 24 h, filtered and then dried overnight in the oven at 80 °C. Chloride salts of multivalent cations were selected because they introduce surface functional groups and active sites that enhance nutrient adsorption [27,28]. In particular, Mg^{2+} promotes P retention through precipitation of magnesium phosphates on the biochar surface, while Al^{3+} enhances the affinity for P and N due to the generation of positively charged surface sites [27,28]. The treated samples were subsequently pyrolyzed in a laboratory furnace from Thermolab under a N atmosphere maintained by 30 mL/min of N_2. The heating rate, pyrolysis temperature and timing matched those used for the BCO_2 biochar. All biochars were produced by applying the same pyrolysis temperature and time, in order to better isolate the effect of physical and chemical activations on nutrient adsorption. Following pyrolysis, all biochars were washed with deionized water until the pH of the filtrate stabilized, and then dried overnight at 80 °C, thereby reducing potential free aluminum and chloride residues. The materials were ground using a mortar, sieved to a particle size smaller than 100 µm, and stored in sealed plastic bags until further use.

2.3. Physicochemical and Morphological Characterizations

Structural characterization was performed on all initially prepared biochars, as well as on those containing nutrients that exhibited the best results following adsorption optimization. All analyses were carried out on the previously sieved biochars with particle sizes < 100 µm. Proximate analysis, encompassing the measurement of moisture content, volatile matter and ash, was done in triplicate according to the ASTM D1762-84 standard [29] developed for the chemical analysis of wood charcoal. Proximate analysis was also performed on the milled vineyard prunings to enable comparison between the raw material and the produced biochars. Textural properties, namely apparent surface area (S_{BET}) and total pore volume (V_{total}), were determined from nitrogen adsorption–desorption isotherms at −196 °C using a TriStar II plus apparatus (Micromeritics). Prior to analysis, all biochar samples (<100 µm) were degassed under nitrogen flow at 200 °C for 12 h to remove adsorbed moisture and volatiles. S_{BET} was calculated using the BET method in the BET method in the relative pressure range 0.05–0.30. V_{total} was estimated from the N adsorbed at $P/P_0 \approx 0.99$. Pore size distributions were obtained from the desorption branch of the isotherm. Surface functional groups were analyzed by FTIR using the KBr pellet method, with a scan range of 350–4000 cm^{-1} and a resolution of 1 cm^{-1} [30]. Surface morphology was examined using scanning electron microscopy/energy dispersive spectroscopy (SEM/EDS) at Centro de Materiais da Universidade do Porto (CEMUP). The analysis was performed using a high-resolution (Schottky) environmental SEM with X-Ray microanalysis and electron backscattered diffraction analysis: FEI Quanta 400 FEG ESEM/EDAX Genesis X4M. Samples were coated with an Au/Pd thin film by sputtering using the SPI module sputter coater equipment. Thermogravimetric analysis (TGA) was performed in Hitachi STA7200RV equipment, between 20 and 800 °C, with a heating rate of 10 °C/min, under a nitrogen flux of 200 mL/min. The pH of biochars was measured using a glass electrode (detection limit of 0.01 pH units) with a biochar-to-water ratio of 1:20 (*w*/*v*) [31,32]. Zeta potential in function of pH was determined using a Malvern Zetasizer Nano ZS (model ZEN3500, Malvern, United Kingdom) equipped with a folded capillary zeta cell (DTS1070). For these measurements, biochar suspensions were prepared in ultrapure water, and pH adjustments were made using 0.1 M HCl and 0.1 M NaOH.

2.4. Adsorption Experiments

2.4.1. Effect of pH on Nutrients Adsorption

The effect of pH on nutrient adsorption was evaluated following methodologies adapted from Khan et al. [11] and Wang et al. [14]. For N adsorption, 1 g of biochar was added to 100 mL of a $NaNO_3$ solution (50 mg/L) and stirred at 400 rpm for 1 h at room temperature to allow initial pH stabilization. After this pre-equilibration step, the pH of the suspensions was adjusted to values ranging from 2 to 13 using either 1 M HCl or 1 M NaOH. The samples were then stirred continuously at 400 rpm for 24 h at room temperature. Subsequently, the mixtures were filtered using 0.22 µm nylon syringe filters, and the resulting solutions were stored in the fridge for a maximum of 24 h prior to analysis. The same procedure was performed for P and K adsorption, using KH_2PO_4 (50 mg/L) or KCl (50 mg/L) solutions, respectively, in place of $NaNO_3$.

The concentration of N in solution was quantified using a total organic carbon analyzer (TOC-VCSN, SHIMADZU, Kyoto, Japan) equipped with the TNM-1 total N module, which determines total N via chemiluminescence detection. P content was determined by UV spectrophotometry (Evolution 300 UV-VIS spectrophotometer, Thermo scientific, Waltham, MA, USA) using the ascorbic acid method. In this method orthophosphate reacts with ammonium molybdate and antimony potassium tartrate under acidic conditions to form phosphomolybdic complex, which is reduced by ascorbic acid to produce a blue color. Absorbance was measured at 880 nm using a spectrophotometer with a 1 cm light path. and K content was assessed by atomic absorption spectrometry (contrAA 700, Analytik Jena GmbH, Jena, Germany). Blanks for each nutrient solution were prepared by stirring the respective solutions under identical conditions (24 h at 400 rpm and room temperature) without biochar. Experiments were performed in duplicate for each tested condition, and the results were expressed in mg of adsorbed nutrient per g of biochar as a function of pH.

2.4.2. Effect of Adsorbent Dosage

Based on the results obtained in Section 2.4.1, further optimizations were carried out for N adsorption at pH 2 using BIMF and for P adsorption at pH 8 using the $BMgCl_2$. In the case of K, due to its limited adsorption performance (see Figure S4 in the Supplementary Materials), no further optimization studies were conducted. The influence of adsorbent dosage on nutrient adsorption was investigated by varying the amount of biochar from 0.0625 to 2.5 g, while maintaining the remaining experimental conditions described in Section 2.4.1. and the respective optimal pH values. A blank was obtained under the same conditions but without biochar addition. Experiments were performed duplicate for each tested condition, and the results were expressed in mg of adsorbed nutrient per g of biochar in function of the adsorbent dosage.

2.4.3. Kinetic Assays

Following the results obtained in Section 2.4.2, kinetic adsorption assays were performed using 1 g of BIMF per 100 mL of $NaNO_3$ (50 mg/L) at pH 2 and 0.5 g of $BMgCl_2$ per 100 mL of KH_2PO_4 (50 mg/L) at pH 8. The experiments were conducted under the same conditions previously described, except for varying contact times, which ranged from 0.5 to 24 h. For each tested time point, a blank was prepared under identical conditions but without biochar. Experiments were performed in duplicate, and the results were expressed in mg of adsorbed nutrient per g of biochar as a function of contact time.

2.4.4. Adsorption Isotherms

Adsorption isotherm experiments were conducted by varying the initial concentration of N and P, ranging from 2.5 to 90 mg/L, while maintaining the previously optimized

experimental conditions for each nutrient. For each concentration, a blank was included under identical conditions but without the biochar addition. Experiments were performed in duplicate for each tested condition, and the results were expressed in mg of adsorbed nutrient per g of biochar as a function of the initial N and P concentration.

The maximum adsorption capacities of the selected biochars were determined by applying the commonly used Langmuir and Freundlich isotherm models. The models are expressed by Equations (1) and (2) [33].

$$\frac{Ce}{Qe} = \frac{Ce}{Qm} + \frac{1}{K_L.Q_m} \text{Langmuir} \quad (1)$$

$$\ln Qe = \ln K_F + \frac{1}{n} \ln Ce \ \text{Freundlich} \quad (2)$$

In the equations, Ce (mg/L) was the equilibrium concentration, Qe (mg/g) corresponds to the amount of nutrient adsorbed in equilibrium, Qm (mg/g) is the Langmuir maximum adsorption capacity K_L (L/mg) is the Langmuir constant related to adsorption rate. For the Freundlich model, K_F $((mg/g)/(L^3mg^{-1})^{-n})$ is the adsorption capacity constant, and n the adsorption intensity constant.

Isotherm parameters and correlation coefficients (R^2) for Langmuir and Freundlich models were obtained by OriginPro 2024b software.

3. Results

3.1. Physicochemical and Morphological Characterizations

The results of the proximate analysis of vineyard prunings (raw material) and the prepared biochars are summarized in Table S1 (Supplementary Materials), which also includes the textural characterization. The raw material exhibited the highest volatile matter content (89.87 ± 1.83%) and the lowest fixed carbon content (5.14 ± 0.88%). Among the biochars, BCO_2 displayed the lowest moisture content (3.11 ± 0.37%) and fixed carbon content (14.16 ± 0.60%), together with the highest volatile matter (80.96 ± 1.01%). $BMgCl_2$ showed the highest values for moisture (8.04 ± 0.23%) and fixed carbon (21.68 ± 0.73%) contents and the lowest volatile matter (69.53 ± 0.67%). BIMF and $BAlCl_3$ presented similar volatile matter and fixed carbon values to BCO_2, although $BAlCl_3$ had the highest moisture among them. Textural properties, including S_{BET} and pore volume, are also presented in Table S1. BIMF and the chemically modified biochars ($BAlCl_3$ and $BMgCl_2$) exhibited comparable S_{BET} (4.60–5.93 m^2/g) and total pore volume (0.00234–0.00524 cm^3/g) values. $BAlCl_3$ exhibiting the highest S_{BET} and $BMgCl_2$ the highest V_{total}. BCO_2 showed the lowest surface area (1.80 m^2/g) and pore volume (0.00104 cm^3/g).

The FTIR spectra of the produced biochars (Figure S1) revealed broad peaks around 3400 cm^{-1} corresponding to stretching vibrations of hydrogen-bonded hydroxyl groups (-OH) and amines (-NH_2). This peak was more intense for $BMgCl_2$ and $BAlCl_3$. Bands at 2920 and 2850 cm^{-1} corresponded to aliphatic C–H deformation vibrations, while bands in the range 1600–1620 cm^{-1} indicated aromatic C=O ring stretching. All biochars showed bands between 1385–1440 cm^{-1}, indicating the presence of methyl (-CH_3) and carboxylic acid groups (-COOH). A small peak at 1035 cm^{-1} was observed only in $BMgCl_2$, assigned to C–O–C stretching vibrations.

The SEM images and EDS spectra of BIMF (Figure 2) and other biochars (Figure S2) revealed characteristic porous structures typical of lignocellulosic feedstocks. BIMF and BCO_2 exhibited shiny surface deposits identified as calcium in BIMF (Figures 2–4) and Ca–P–K mixtures in BCO_2 (Figure S2(a4)). $BAlCl_3$ (Figure S2(b1,b2)) showed surface deposits of aluminum oxide (AlO), while $BMgCl_2$ exhibited nanoflake structures identified as magnesium oxide (MgO).

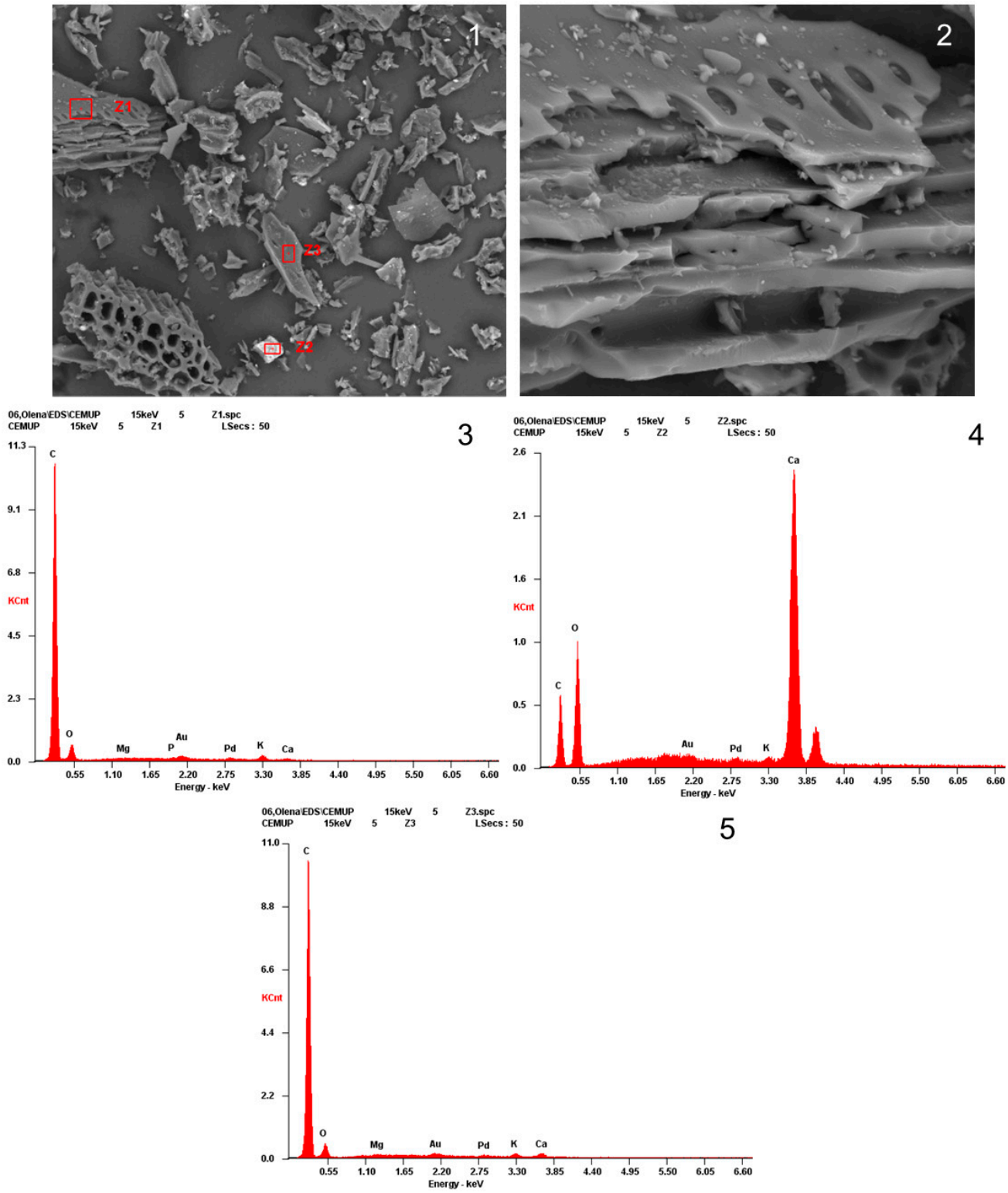

Figure 2. SEM images acquired in backscattered electron mode at different magnifications: (**1**) 1000× and (**2**) 5000×. Corresponding EDS spectra collected from selected points in the SEM images: (**3**) spectrum from point Z1, (**4**) spectrum from point Z2, and (**5**) spectrum from point Z3 of BIMF (biochar prepared at the *Ibero Massa Florestal* company).

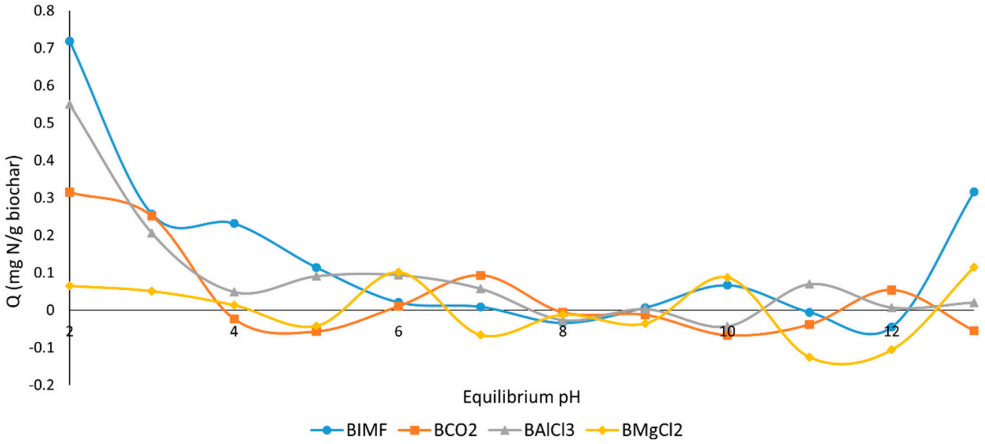

Figure 3. The effect of pH on nitrogen (N) adsorption for the BIMF (biochar prepared at Ibero Massa Florestal company), BCO_2 (biochar prepared with a flux of CO_2), $BAlCl_3$ (biochar pretreated with $AlCl_3$) and $BMgCl_2$ (biochar pretreated with $MgCl_2$).

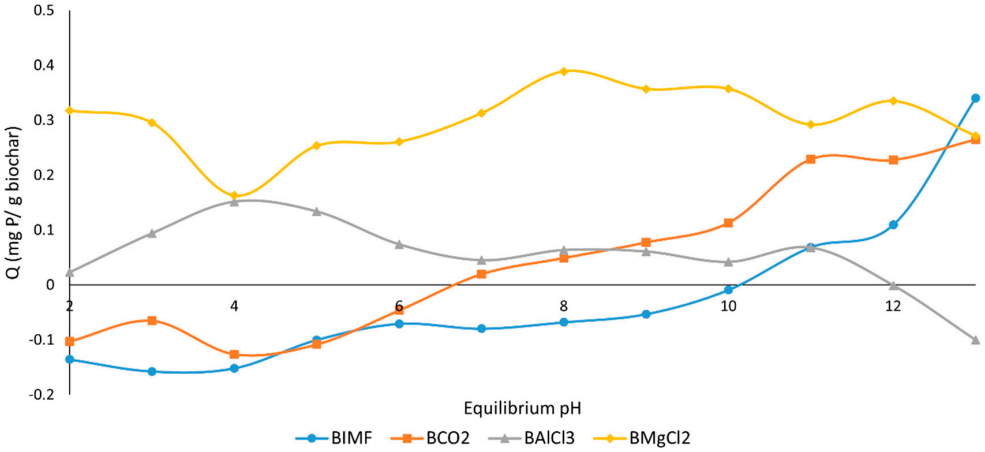

Figure 4. The effect of pH on phosphorous (P) adsorption for the BIMF (biochar prepared at Ibero Massa Florestal company), BCO_2 (biochar prepared with a flux of CO_2), $BAlCl_3$ (biochar pretreated with $AlCl_3$) and $BMgCl_2$ (biochar pretreated with $MgCl_2$).

TGA analysis (Figure S3) showed an initial weight loss between 24–200 °C, corresponding to residual water removal. This weight loss ranged from 2.6% in BCO_2 to 8.4% in $BMgCl_2$. The second stage (200–500 °C) reflected the gradual decomposition of lignin and cellulose. BIMF had the greatest thermal stability, with only 3.8% mass loss, while other biochars lost between 7.6 and 12.6%. Above 500 °C, the remaining decomposition involved breakdown of more stable carbon frameworks. Weight loss ranged from 7.5% in BIMF-N to 13.3% in $BMgCl_2$.

The relationship between zeta potential and pH (Figure S4) showed that all biochars were negatively charged across the tested pH range. $BMgCl_2$ exhibited the least variation in zeta potential across the pH range, while $BAlCl_3$ showed larger changes with pH.

3.2. Effect of pH on Nutrients Loading

The influence of pH on N adsorption was investigated for all prepared biochars (BIMF, BCO_2, $BAlCl_3$, and $BMgCl_2$), and the results are presented in Figure 3. Under certain pH values, several biochars exhibited a net release of N into the solution rather than adsorption. Among the tested materials, BIMF and $BAlCl_3$ demonstrated the highest N retention at pH 2, with maximum adsorption capacities of 0.72 mg N g^{-1} and 0.55 mg N g^{-1}, respectively. $BMgCl_2$ exhibited lower N adsorption values, reaching a maximum of 0.11 mg N g^{-1} at pH 13. Based on these results, BIMF was selected for subsequent N adsorption optimization

experiments. Beyond its adsorption performance, BIMF also offers a practical advantage since it is produced industrially by Ibero Massa Florestal, supporting potential scalability for large-scale applications.

The effect of pH on P adsorption for all biochars (BIMF, BCO_2, $BAlCl_3$, and $BMgCl_2$) is shown in Figure 4. BCO_2 released P into the solution between pH 2–7, and BIMF between pH 2–10. As pH increased, P adsorption also increased, reaching maximum values of 0.26 mg P g^{-1} and 0.34 mg P g^{-1} for BCO_2 and BIMF, respectively, at pH 13. For the chemically modified biochars, distinct responses were observed. P adsorption by $BAlCl_3$ remained low and largely independent of pH. In contrast, $BMgCl_2$ showed a progressive increase in P adsorption starting at pH 3 and stabilizing around pH 8 with 0.39 mg P g^{-1} biochar. SEM images (Figure S2) indicated phosphate-containing precipitates on $BMgCl_2$ surfaces and at the bottom of the adsorption solutions. Despite similar maximum P adsorption capacities between BIMF and $BMgCl_2$, the latter was chosen for further P adsorption optimization due to its peak performance under moderately alkaline conditions (pH 8), which are easier to maintain than the strongly alkaline environment (pH 13) required for BIMF.

K adsorption as a function of pH for all tested biochars is presented in Figure S5. Overall, the biochars showed very limited K retention. Only BCO_2 displayed measurable K adsorption between pH 7 and 11, reaching a maximum of 0.098 mg K g^{-1} at pH 8. For all biochars, a consistent K release into the solution was observed, particularly for BIMF. Given the low K adsorption and predominance of nutrient release, no further K adsorption optimization experiments were conducted.

3.3. Effect of Adsorption Dosage

The influence of biochar dosage on nutrient uptake was evaluated by varying the mass of biochar added to 100 mL of solution under the previously optimized pH conditions (pH 2 for N with BIMF; pH 8 for P with $BMgCl_2$). Figure 5 illustrates the effect of adsorbent loading on nutrient adsorption capacity. For N adsorption (Figure 5a), the adsorption capacity increased slightly as the BIMF dosage rose from 0.125 g to 0.500 g, reaching a maximum at 0.500 g. Beyond this point, a gradual decrease in N adsorption per gram of biochar was observed. Although the total nutrient uptake increased with higher biochar mass, the uptake normalized per gram of biochar declined. For P adsorption (Figure 5b), the adsorbed amount (mg P g^{-1} biochar) decreased continuously as $BMgCl_2$ dosage increased from 0.0625 g to 2.5 g. However, P uptake per gram was nearly identical at 0.125 g and 0.250 g dosages. Based on these results, 0.500 g BIMF per 100 mL solution was selected for subsequent N adsorption experiments, and 0.250 g $BMgCl_2$ per 100 mL solution for P adsorption, as both represented the points of maximum normalized uptake.

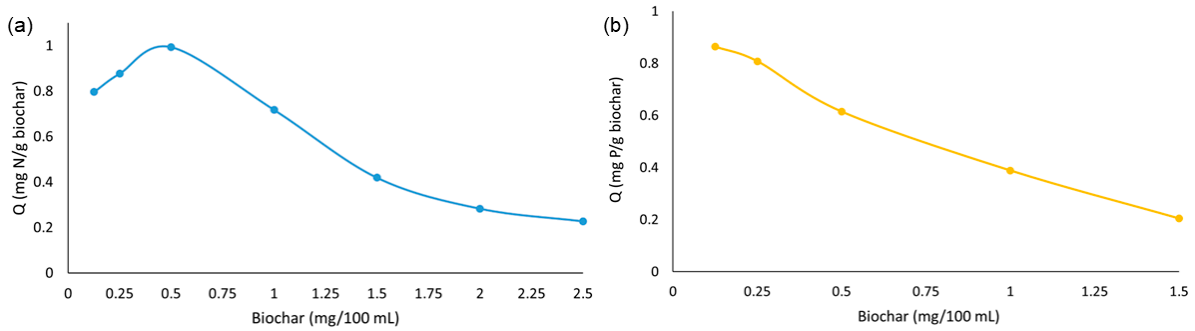

Figure 5. Adsorption of nitrogen (N) (**a**) and phosphorus (P) (**b**) in function of the amount of biochar added to the solution.

3.4. Kinetic Assays

The temporal evolution of N and P adsorption onto biochars is presented in Figure 6. As shown in Figure 6a, N adsorption exhibited a rapid initial uptake within the first 15 min (0.25 h) following pH adjustment, indicating a high initial adsorption rate. It is important to note that this period is measured after pH stabilization, and some nutrient uptake may have occurred during the pH adjustment stage. Following the initial surge, N adsorption gradually increased over the next 4 h and then slightly declined, reaching equilibrium at approximately 8 h. In contrast, P adsorption (Figure 6b) showed a steady, nearly linear increase throughout the 24 h experimental period without reaching a clear equilibrium. The maximum adsorption capacities observed were 1.15 mg N g^{-1} biochar after 4 h and 0.81 mg P g^{-1} biochar after 24 h. Based on these results, contact times of 4 h for N adsorption and 24 h for P adsorption were selected for subsequent optimization experiments.

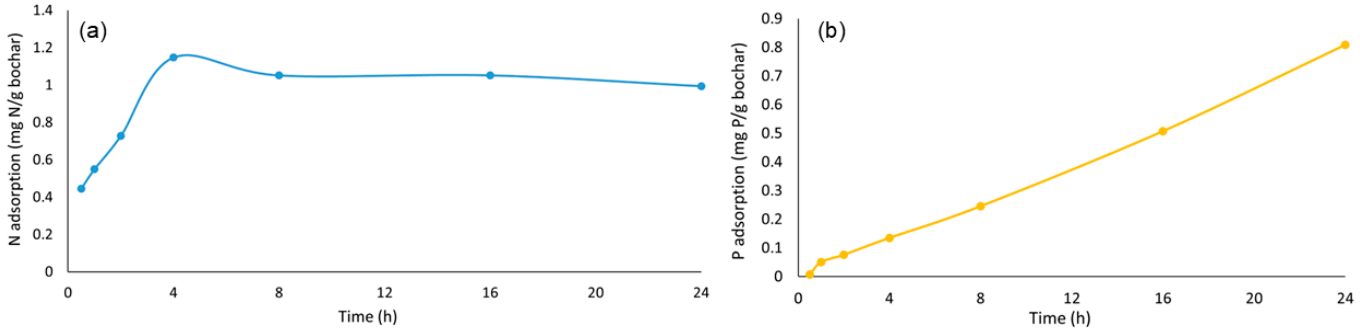

Figure 6. Effect of time on nitrogen (N) (**a**) and phosphorus (P) (**b**) adsorption.

3.5. Adsorption Isotherms

The adsorption isotherms for N and P are presented in Figures S6 and S7 (Supplementary Materials), respectively. At low nutrient concentrations, the adsorption capacity of both biochars increased sharply, indicating the availability of numerous active sites on the biochar surface. As the initial concentration rose, the adsorption rate gradually decreased and reached a plateau, suggesting that the adsorption sites became progressively saturated or blocked—a behaviour commonly reported in adsorption systems [6,33]. As summarized in Table S2 (Supplementary Materials), both the Freundlich and Langmuir isotherm models provided satisfactory fits to the experimental data. The coefficients of determination (R^2) corresponded to 0.87 and 0.86, for N and P adsorption, respectfully, in the Freundlich model. Nevertheless, for both N and P, the Langmuir model provided a superior fit, with R^2 being 0.94 and 0.90 for N and P adsorption, respectfully. According to this model, the maximum adsorption capacities (Q_m) were 10.4 mg N g^{-1} biochar and 12.7 mg P g^{-1} biochar for BIMF and $BMgCl_2$, respectively.

3.6. Structural Characterization of Biochars After Nutrients Adsorption

To assess the impact of nutrient adsorption on the physicochemical properties of the biochars, the optimized samples (BIMF–N and $BMgCl_2$–P) were characterized using the same analytical techniques as those applied to the original materials. The proximate analysis results are summarized in Table S1 (Supplementary Materials).

The moisture content of BIMF–N was 3.89 ± 0.27%, while $BMgCl_2$–P had a moisture content of 11.12 ± 0.89%. These values were comparable to those of the pre-adsorption biochars. Fixed carbon content remained largely unchanged for BIMF–N but increased slightly for $BMgCl_2$–P. Volatile matter decreased in $BMgCl_2$–P, and changed minimally for BIMF–N. The S_{BET} increased notably following adsorption—approximately 2-fold for BIMF–N and 5.8-fold for $BMgCl_2$–P. The FTIR spectra (Figure S1, Supplementary Materials) revealed a pronounced peak near 3400 cm^{-1} in $BMgCl_2$–P, attributed to water absorp-

tion during KBr pellet preparation. A strong band at 1035 cm^{-1} (C–O–C stretching of cellulose/hemicellulose) was present in $BMgCl_2$–P and weaker in BIMF–N. Additionally, BIMF–N showed a band near 875 cm^{-1}, associated with C–H wagging vibrations in aromatic and heteroaromatic structures. SEM and EDS analyses (Figure S8, Supplementary Materials) revealed visible structural changes after adsorption. The BIMF–N surface appeared smoother, and Ca was not detected by EDS (Figure S8(a3,a4)). In contrast, $BMgCl_2$–P displayed distinct solid precipitates separated from the biochar matrix. EDS spectra (Figure S8(b3)) showed that these precipitates were enriched in Mg, O, and P and contained minimal C. TGA analysis (Figure S3, Supplementary Materials) showed an initial weight loss between 24–200 °C for both post-adsorption biochars, corresponding to moisture removal. In the second stage, BIMF–N exhibited a minor weight loss (3.2%) compared to the more substantial loss observed for $BMgCl_2$–P (12.6%). At temperatures above 500 °C, both samples displayed slightly lower total weight losses than their pre-adsorption counterparts.

4. Discussion

4.1. Physicochemical and Morphological Characterizations

The higher moisture content of the chemically modified biochars suggests an increased hydrophilic character and surface polarity, which may enhance water retention and, consequently, adsorption capacity. The observed volatile matter and fixed carbon values align with previous reports for biochars from cellulosic materials produced at low pyrolysis temperatures, such as wheat straw, platane wood, and oak biochars [11,34]. Interestingly, despite the longer holding time (14 h) during BIMF production, its surface area was not significantly higher than that of the chemically modified biochars, which underwent only 1 h of pyrolysis. In contrast, Wu et al. [13] found much lower volatile matter contents for rice straw biochars produced at 700 °C. These comparisons emphasize the strong influence of pyrolysis temperature on carbonization and volatile removal, with higher temperatures promoting fixed carbon formation. The relatively low fixed carbon and high volatile matter contents of vineyard pruning biochars produced in this study at 400 °C are therefore consistent with the moderate pyrolysis conditions, indicating partial carbonization that may limit surface area development.

Comparable S_{BET} values have been reported for other agricultural residues, such as wheat straw and pinewood biochars (1.1–4.1 $m^2\ g^{-1}$) [9,11]. However, higher values (18.9–420.9 $m^2\ g^{-1}$) have been observed for sugar beet tailings, peanut shells, and hickory wood chip biochars treated with $MgCl_2$ or $AlCl_3$ [27,28]. The relatively low surface areas of vineyard pruning biochars likely result from the moderate pyrolysis temperature, which limits volatile removal and pore development [25]. This interpretation is consistent with their high volatile content and low fixed carbon levels.

The FTIR data further confirm the presence of oxygenated functional groups (–OH, –COOH, C=O, COO^-), which may enhance adsorption via hydrogen bonding and electrostatic interactions [13]. The distinct 1035 cm^{-1} band in $BMgCl_2$ indicates residual cellulose and hemicellulose structures, suggesting incomplete decomposition during pyrolysis.

The SEM–EDS analyses support successful surface modification of biochars. The presence of AlO and MgO deposits indicates effective incorporation of metal-based species, which could enhance adsorption via ion exchange and surface complexation. Similar surface modifications have been associated with improved nutrient retention in other studies [35]. These morphological features have practical significance for adsorption efficiency, as the observed pores, surface roughness, and metal oxide deposits increase the number of available active sites, facilitating nutrient retention via electrostatic interactions, surface complexation, and precipitation.

The TGA results corroborate the proximate and FTIR data: chemically modified biochars exhibited higher weight loss due to their greater content of labile, oxygenated groups. Comparable trends have been reported by Biswas et al. [9], who observed reduced thermal stability in hydrophilic, metal-modified biochars. While this chemical functionalization enhances surface polarity and the availability of adsorption sites, the reduced thermal stability indicates these labile groups may be sensitive to environmental conditions such as moisture, pH, and soil interactions. Therefore, TGA not only confirms the presence of active functional groups but also highlights their potential impact on adsorption efficiency and the stability of the biochar when applied as a soil amendment.

Finally, the negative zeta potentials across the pH range confirm the inherently anionic nature of the biochars, which may limit adsorption of negatively charged ions [9]. The lower pH-dependence of $BMgCl_2$ zeta potential suggests more stable, non-protonating surface groups such as MgO, while the stronger pH response of $BAlCl_3$ indicates the presence of Al–OH or AlOOH moieties susceptible to protonation [31]. These findings emphasize how surface functionalization modulates electrochemical behaviour and potential adsorption mechanisms.

4.2. Effect of pH on Nutrients Loading

The adsorption of nutrients onto biochars is strongly influenced by pH, as it determines both the ionization state of nutrient species and the surface charge of the adsorbent [33]. At low pH, protonation of surface functional groups increases positive charge and favours adsorption of anionic species, whereas at high pH, deprotonation generates a negatively charged surface that enhances cation uptake. These shifts directly affect adsorption efficiency by modulating electrostatic attraction, ion exchange, and surface complexation. Therefore, identifying the optimal pH range is essential for maximizing the biochar adsorption of nutrients.

The observed net N release at certain pH levels aligns with findings by Li, Galoustian, and Trejo [35], who reported nitrate desorption from biochars when native nutrient content exceeded the adsorptive capacity under test conditions. The limited N adsorption under most pH conditions can be attributed to the electrostatic repulsion between negatively charged nitrate ions (NO_3^-) and the negatively charged biochar surfaces, as confirmed by the zeta potential measurements (Figure S4). At pH 2, however, the surface charge of BIMF, BCO_2, and $BAlCl_3$ approached neutrality, which reduced electrostatic repulsion and enabled alternative adsorption mechanisms such as ligand exchange, hydrogen bonding, or pore entrapment [36]. The higher N adsorption observed for BIMF and $BAlCl_3$ suggests that specific surface functional groups facilitate these non-electrostatic interactions. In contrast, $BMgCl_2$ showed weak N adsorption, consistent with its relatively stable negative surface potential that limits NO_3^- association. While numerous studies have explored N-enriched biochars [10,27,33,35,37], few have examined the pH-dependent mechanisms influencing N uptake. This study therefore provides novel insights into pH-driven N–biochar interactions, highlighting that acidic conditions can temporarily overcome electrostatic barriers to enable adsorption.

For P adsorption, the contrasting behaviours between unmodified and chemically modified biochars reflect differences in surface chemistry. The P release observed under acidic to near-neutral pH for BIMF and BCO_2 suggests the leaching of inherent P species, which dominates over adsorption at lower pH. The gradual P adsorption increase at higher pH is likely associated with the transformation of phosphate species in function of pH, more precisely to $H_2PO_4^-$ (pH 2.13–7.20), HPO_4^{2-} (pH 7.20–12.33), and PO_4^{3-} (pH $\geq$ 12.33) [38], and the activation of surface complexation and precipitation mechanisms rather than electrostatic attraction. For $BMgCl_2$, the enhanced P adsorption at alkaline pH can be explained by the formation of magnesium–phosphate precipitates,

a mechanism well-documented in the literature [8]. SEM images support this interpretation, revealing solid phosphate deposits both on the $BMgCl_2$ surface and in the bulk solution. Similar results were reported by Deng et al. [39], who found greater P adsorption at pH 7–11 for Mg^{2+}-supported biochars. These parallels confirm that Mg-modification enhances P affinity via surface precipitation and complexation. Despite this improvement, $BMgCl_2$ maximum P adsorption capacity (0.39 mg P g^{-1}) remains below that reported for $ZnCl_2$- or coal-gangue-modified biochars, which achieved up to 0.99 mg P g^{-1} [9] and 7.8 mg P g^{-1} [14], respectively. These discrepancies are primarily attributed to the lower surface area of vineyard-pruning biochars ($\leq$6 m^2 g^{-1}), which restricts active site availability. Thus, while Mg-loading is effective, combining it with surface activation or higher pyrolysis temperatures could significantly enhance P adsorption capacity.

For K adsorption, all biochars exhibited weak retention and in many cases net K release, indicating poor binding affinity for K^+. The strong release from BIMF suggests that vineyard pruning residues inherently contain bioavailable K, making these biochars more suitable as nutrient sources rather than K adsorbents. The lack of significant pH dependence in K adsorption further supports that K^+ interactions with these materials are minimal and dominated by ion exchange or leaching processes rather than specific adsorption. Comparable findings have been reported for low-surface-area biochars [40].

Overall, the pH-dependent adsorption behaviour of N, P, and K on vineyard pruning biochars underscores the complex interplay between surface chemistry, charge properties, and mineral composition. The results identify BIMF and $BMgCl_2$ as the most promising candidates for targeted N and P removal, respectively, with strong potential for practical application due to their scalability and moderate operational requirements.

4.3. Effect of Adsorption Dosage

The observed relationship between biochar dosage and adsorption capacity reflects a common behaviour in adsorbent systems. At low dosages, the increase in available surface area enhances the probability of adsorbate–adsorbent interactions, leading to higher uptake per unit mass. However, at higher dosages, particle aggregation, site overlap, and incomplete utilization of available active sites reduce the effective surface area and lead to a decline in adsorption capacity per gram.

This trend was also reported by Biswas et al. [9], who observed a reduction in P uptake from 4.6 to 0.5 mg P g^{-1} as biochar dosage increased from 0.1 to 1 g per 100 mL, even though total removal efficiency rose from 92 to 100%. Similarly, Wang et al. [14] reported a decrease in P uptake from 9.5 to 4.0 mg PO_4^{3-} g^{-1} when dosage increased from 0.125 to 2.5 g per 100 mL (50 mg L^{-1} KH_2PO_4). The consistency of these findings with the present results indicates that the trade-off between per-gram adsorption capacity and overall removal efficiency is a general characteristic of nutrient–biochar systems.

Therefore, selecting an optimal dosage is essential to balance efficiency and material utilization. The chosen dosages (0.500 g BIMF for N and 0.250 g $BMgCl_2$ for P) provide the best compromise between maximizing per-gram adsorption capacity and ensuring sufficient total nutrient removal for practical applications.

4.4. Kinetic Assays

The rapid initial adsorption of N observed within the first 15 min indicates that easily accessible surface sites were quickly occupied, consistent with adsorption driven primarily by electrostatic interactions. This behaviour parallels that reported by Vamvuka et al. [33], who observed a similar two-stage pattern during ammonium adsorption by potassium hydroxide-modified almond kernel biochar. The subsequent gradual approach

to equilibrium and slight decline after 4 h suggest partial desorption or redistribution of N ions as equilibrium conditions were established.

The kinetic pattern of P adsorption, on the other hand, reflects a slower and more progressive mechanism. The near-linear increase over 24 h without an apparent equilibrium suggests that intraparticle diffusion and surface precipitation were the dominant processes, as also proposed by Wu et al. [8]. Comparable behaviour was reported by Biswas et al. [9], where extending the contact time beyond 24 h did not significantly enhance P uptake, indicating a plateau effect once the surface became saturated or precipitation equilibria were reached.

Differences between the kinetic profiles of N and P adsorption likely arise from the distinct physicochemical interactions of these ions with the biochar surfaces. Nitrate adsorption relies mainly on electrostatic and hydrogen-bonding interactions, which occur rapidly, whereas phosphate adsorption involves ligand exchange and precipitation reactions that proceed more slowly. The slower kinetics of P adsorption observed here differ from the faster uptake reported by Wang et al. [14] for coal gangue-modified oilseed rape biochar, likely due to variations in biochar mineral composition, surface area, and the availability of reactive metal sites.

Overall, the kinetic analysis highlights that while N adsorption on BIMF is rapid and occurs on the surface, P adsorption on $BMgCl_2$ is diffusion- and precipitation-controlled. These differences justify the selected equilibrium contact times—4 h for N and 24 h for P—for subsequent optimization and isotherm studies.

4.5. Adsorption Isotherms

The strong correlation with the Langmuir model (R^2 = 0.94 for N adsorption and R^2 = 0.90 for P adsorption) suggests that nutrient uptake was dominated by specific, energetically uniform sites, supporting a monolayer adsorption mechanism without significant interactions between adsorbed species [8,41]. This observation implies that both N and P adsorption on the studied biochars are controlled mainly by chemisorption or surface complexation processes rather than multilayer physical adsorption.

The maximum adsorption capacity obtained for BIMF (10.4 mg N g^{-1}) was approximately 1.3 times higher than the value reported by Li et al. [35] for solar-radiated guava wood chip biochar, confirming the relatively high N retention potential of vineyard pruning–derived biochar. Similarly, the Q_m; value of 12.7 mg P g^{-1} achieved for $BMgCl_2$ surpassed the values reported by Wang et al. [14] and Biswas et al. [9] (7.9 and 10.4 mg P g^{-1}, respectively) for coal gangue-modified and $ZnCl_2$–calcinated pinewood biochars.

Comparable results were observed by Wu et al. [8] for pristine peanut shell biochar (12.87 mg P g^{-1}), while their $MgCl_2$-modified counterpart exhibited an even higher adsorption capacity (18.94 mg P g^{-1}). Although the $BMgCl_2$ used in this study achieved slightly lower values, the performance is notable given the much lower S_{BET} of vineyard pruning biochars. The lower S_{BET} limits the total number of available adsorption sites, which partially explains the differences compared with higher-performing feedstocks.

In more complex systems, such as secondary treated wastewater, Zheng et al. [28] reported a lower Q_m of 8.35 mg P g^{-1}, underscoring the impact of competing ions and organic matter on adsorption performance. In contrast, Biswas et al. [10] and Zhang et al. [27] reported considerably higher P capacities (64.45 and 159 mg P g^{-1}, respectively) for biochars derived from pine bark and sugar beet tailings modified with $MgCl_2 \cdot 6H_2O$, again emphasizing the influence of feedstock composition, porosity, and modification protocols.

Despite not reaching the highest reported adsorption capacities, the vineyard pruning-based biochars demonstrated promising adsorption efficiencies considering their modest surface areas and the low-cost, renewable nature of the feedstock. These findings highlight

their potential as sustainable nutrient adsorbents for environmental applications. Future research should investigate the influence of pyrolysis temperature and residence time on surface development and porosity to further enhance adsorption performance.

4.6. Structural Characterization of Biochars After Nutrients Adsorption

The characterization results demonstrate that nutrient adsorption led to both chemical and structural modifications in the biochars. The increase in fixed carbon and the decrease in volatile matter, particularly for $BMgCl_2$–P, suggest that extended stirring and adsorption contact contributed to the removal of weakly bound organics and the exposure of new active sites, which is reflected in the higher BET surface areas. Similar increases in S_{BET} following adsorption were reported by Biswas et al. [9] for $ZnCl_2$-modified pinewood biochars, attributed to surface cleaning during agitation.

The FTIR spectra corroborate these surface modifications, as the emergence and variation of functional group bands (notably near 1035 cm^{-1} and 875 cm^{-1}) indicate alterations in surface oxygenated and aromatic structures due to adsorption.

SEM–EDS analyses highlighted distinct nutrient retention mechanisms in BIMF–N and $BMgCl_2$–P. In BIMF–N, nitrogen was mainly adsorbed onto the biochar surface, while the absence of Ca suggests that desorption or dissolution of surface minerals occurred simultaneously, contributing to a smoother surface. In contrast, $BMgCl_2$–P exhibited well-defined Mg–O–P-rich precipitates. This elemental composition is characteristic of magnesium phosphate phases, indicating that phosphorus removal in this system was largely driven by precipitation rather than surface adsorption alone. This aligns with mechanisms proposed by Xu et al. [42] and Biswas et al. [9], where phosphate ions react with Mg^{2+} to form stable precipitates such as $Mg_3(PO_4)_2$, $MgHPO_4$ or $Mg(H_2PO_4)_2$. These findings validate that $BMgCl_2$ functions via a dual mechanism combining electrostatic attraction and surface/bulk precipitation.

The smoother surfaces observed in SEM images after adsorption likely result from abrasion and particle detachment during the stirring process, consistent with the cleaning hypothesis supported by BET data [35]. TGA analysis confirms that post-adsorption biochars possess enhanced thermal stability, potentially due to a more condensed carbon structure and removal of labile components [9].

Overall, these results demonstrate that adsorption processes not only influenced the nutrient content of the biochars but also modified their surface chemistry and physical structure, thereby potentially enhancing their stability and reusability for future adsorption cycles.

5. Conclusions

This study demonstrated the potential of vineyard prunings as a sustainable feedstock for producing nutrient-enriched biochars suitable for application as EEFs. Clear differences in adsorption performance were observed among the biochars, with solution pH strongly influencing nutrient uptake. BIMF exhibited the highest affinity for N, while $BMgCl_2$ showed superior P adsorption, with maximum Langmuir adsorption capacities of 10.4 mg N/g for BIMF and 12.7 mg P/g for $BMgCl_2$, respectively. SEM–EDS analyses of $BMgCl_2$-P further indicated that P removal occurred through a dual mechanism, combining surface adsorption and precipitation of magnesium phosphate solids. This feature expands the potential applications of $BMgCl_2$, making it not only a candidate for P-enriched fertilizers but also a material of interest for P recovery from wastewater and the remediation of eutrophic systems. In contrast, K adsorption was negligible across all tested biochars, with consistent K release into the solution, suggesting that vineyard pruning-derived biochars may act as a supplementary K source rather than an adsorbent.

Overall, BIMF and $BMgCl_2$ emerge as promising candidates for developing N and P based EFFs, respectively. This work provides the first demonstration of vineyard prunings being valorised into nutrient-retentive biochars through scalable industrial production and targeted chemical modifications. Future studies should investigate nutrient release dynamics in soil systems, as well as impacts on crop productivity and soil health, to validate their agronomic and environmental benefits in real-world conditions.

Supplementary Materials: The following supporting information can be downloaded at: https://www.mdpi.com/article/10.3390/environments12120491/s1, Figure S1—FTIR spectra of BIMF (biochar prepared at Ibero Massa Florestal company), BCO_2 (biochar prepared with a flux of CO_2), $BAlCl_3$ (biochar pretreated with $AlCl_3$), $BMgCl_2$ (biochar pretreated with $MgCl_2$), BIMF-N (biochar prepared at Ibero Massa Florestal after N adsorption) and $BMgCl_2$-P (biochar pretreated with $MgCl_2$ after P adsorption); Figure S2—SEM images acquired in backscattered electron mode and corresponding EDS spectra of: (a) BCO_2 (biochar prepared with a flux of CO_2), (b) $BAlCl_3$ (biochar pretreated with $AlCl_3$) and (c) $BMgCl_2$ (biochar pretreated with MgCl2); Figure S3—TGA graph of BIMF (biochar prepared at Ibero Massa Florestal company), BCO_2 (biochar prepared with a flux of CO_2), $BAlCl_3$ (biochar pretreated with $AlCl_3$), $BMgCl_2$ (biochar pretreated with $MgCl_2$), BIMF-N (biochar prepared at Ibero Massa Florestal after N adsorption) and $BMgCl_2$-P (biochar pretreated with $MgCl_2$ after P adsorption); Figure S4—Zeta potential in relation to the pH value of the solution for the BIMF (biochar prepared at Ibero Massa Florestal company), BCO_2 (biochar prepared with a flux of CO_2), $BAlCl_3$ (biochar pretreated with $AlCl_3$) and $BMgCl_2$ (biochar pretreated with $MgCl_2$); Figure S5—The effect of pH on potassium (K) adsorption for the BIMF (biochar prepared at Ibero Massa Florestal company), BCO_2 (biochar prepared with a flux of CO_2), $BAlCl_3$ (biochar pretreated with $AlCl_3$) and $BMgCl_2$ (biochar pretreated with $MgCl_2$); Figure S6—N adsorption isotherms for BIMF (biochar prepared at Ibero Massa Florestal company); Figure S7—P adsorption isotherms for $BMgCl_2$ (biochar pretreated with $MgCl_2$); Figure S8—SEM images and EDS spectra: (a) BIMF-N (biochar prepared at Ibero Massa Florestal company after N adsorption) and (b) $BMgCl_2$-P (biochar pretreated with $MgCl_2$ after P adsorption); Table S1—Proximate analysis and textural properties and of BIMF (biochar prepared at Ibero Massa Florestal company), BCO_2 (biochar prepared with a flux of CO_2), $BAlCl_3$ (biochar pretreated with $AlCl_3$), $BMgCl_2$ (biochar pretreated with $MgCl_2$), BIMF-N (biochar prepared at Ibero Massa Florestal after N adsorption), $BMgCl_2$-P (biochar pretreated with $MgCl_2$ after P adsorption). Proximate analysis is also presented for the raw material (vineyard prunings). All analysis were performed in triplicate, and the values correspond to the mean of replicates and respective standard deviation, except for textural properties which were analysed only once.; Table S2—Summary of the best-fit isotherm model parameters for N and P adsorption.

Author Contributions: O.D. Conceptualization; Investigation; Methodology; Software; Visualization; Writing—original draft and Writing—review and editing. A.F.P. Methodology; Resources; Software and Writing—review and editing; C.D.-M. Funding acquisition; Investigation; Project administration; Resources and Writing—review and editing; P.M.L.C. Funding acquisition; Project administration; Resources; Supervision and Writing—review and editing. M.M.M. Conceptualization; Investigation; Project administration; Resources; Supervision; Validation; Writing—original draft and Writing—review and editing. All authors have read and agreed to the published version of the manuscript.

Funding: This work received financial support from the PT national funds (FCT/MECI, Fundação para a Ciência e Tecnologia and Ministério da Educação, Ciência e Inovação) through the project UID/50006/2025-Laboratório Associado para a Química Verde—Tecnologias e Processos Limpos. The authors also thank the CBQF scientific collaboration under the FCT project UIDB/50016/2020.

Data Availability Statement: The original contributions presented in this study are included in the article/Supplementary Material. Further inquiries can be directed to the corresponding author.

Acknowledgments: Olena Dorosh (2021.05984.BD) is thankful for her Ph.D. grant financed by FCT/MCTES. Manuela M. Moreira (2023.05993.CEECIND/CP2842/CT0009, DOI: 10.54499/2023.05993.CEECIND/CP2842/CT0009) is thankful for her contract financed by FCT/MCTES—CEEC

Individual Program Contract and to REQUIMTE/LAQV. The supply of the vineyard prunings is acknowledged to Sogrape and the biochar production to Ibero Massa Florestal company.

Conflicts of Interest: The authors declare no conflicts of interest.

Abbreviations

The following abbreviations are used in this manuscript:

$BAlCl_3$	Biochar pretreated with $AlCl_3$
BCO_2	Biochar prepared with a flux of CO_2
BIMF	Biochar industrially produced by Ibero Massa Florestal company
$BMgCl_2$	Biochar pretreated with $MgCl_2$
EEFs	Enhanced efficiency fertilizers
FTIR	Fourier transform infrared spectroscopy
K	Potassium
N	Nitrogen
P	Phosphorous
pHPZC	pH at point of zero charge
SBET	Specific surface area using Brunauer–Emmett–Teller (BET) theory
SEM/EDS	Scanning electron microscopy/energy dispersive spectroscopy
TGA	Thermogravimetric analysis
Vtotal	Total pore volume

References

1. Komnitsas, K.A.; Zaharaki, D. Morphology of modified biochar and its potential for phenol removal from aqueous solutions. *Front. Environ. Sci.* **2016**, *4*, 26. [CrossRef]
2. Tomczyk, A.; Kondracki, B.; Szewczuk-Karpisz, K. Chemical modification of biochars as a method to improve its surface properties and efficiency in removing xenobiotics from aqueous media. *Chemosphere* **2022**, *312*, 137238. [CrossRef]
3. Panahi, H.K.S.; Dehhaghi, M.; Ok, Y.S.; Nizami, A.-S.; Khoshnevisan, B.; Mussatto, S.I.; Aghbashlo, M.; Tabatabaei, M.; Lam, S.S. A comprehensive review of engineered biochar: Production, characteristics, and environmental applications. *J. Clean. Prod.* **2020**, *270*, 122462. [CrossRef]
4. Correia-Sá, L.; Soares, C.; Freitas, O.M.; Moreira, M.M.; Nouws, H.P.A.; Correia, M.; Paíga, P.; Rodrigues, A.J.; Oliveira, C.M.; Figueiredo, S.A.; et al. A three-dimensional electrochemical process for the removal of carbamazepine. *Appl. Sci.* **2021**, *11*, 6432. [CrossRef]
5. Fernandes, M.J.; Moreira, M.M.; Paíga, P.; Dias, D.; Bernardo, M.; Carvalho, M.; Lapa, N.; Fonseca, I.; Morais, S.; Figueiredo, S.; et al. Evaluation of the adsorption potential of biochars prepared from forest and agri-food wastes for the removal of fluoxetine. *Bioresour. Technol.* **2019**, *292*, 121973. [CrossRef] [PubMed]
6. Kamali, M.; Sweygers, N.; Al-Salem, S.; Appels, L.; Aminabhavi, T.M.; Dewil, R. Biochar for soil applications-sustainability aspects, challenges and future prospects. *Chem. Eng. J.* **2022**, *428*, 131189. [CrossRef]
7. Soares, C.; Correia-Sá, L.; Paíga, P.; Barbosa, C.; Remor, P.; Freitas, O.M.; Moreira, M.M.; Nouws, H.P.; Correia, M.; Ghanbari, A.; et al. Removal of diclofenac and sulfamethoxazole from aqueous solutions and wastewaters using a three-dimensional electrochemical process. *J. Environ. Chem. Eng.* **2022**, *10*, 108419. [CrossRef]
8. Wu, L.; Wei, C.; Zhang, S.; Wang, Y.; Kuzyakov, Y.; Ding, X. MgO-modified biochar increases phosphate retention and rice yields in saline-alkaline soil. *J. Clean. Prod.* **2019**, *235*, 901–909. [CrossRef]
9. Biswas, B.; Rahman, T.; Sakhakarmy, M.; Jahromi, H.; Eisa, M.; Baltrusaitis, J.; Lamba, J.; Torbert, A.; Adhikari, S. Phosphorus adsorption using chemical and metal chloride activated biochars: Isotherms, kinetics and mechanism study. *Heliyon* **2023**, *9*, e19830. [CrossRef]
10. Biswas, B.; Adhikari, S.; Jahromi, H.; Ammar, M.; Baltrusaitis, J.; Torbert, A.; Linhoss, J.; Lamba, J. Magnesium doped biochar for simultaneous adsorption of phosphate and nitrogen ions from aqueous solution. *Chemosphere* **2024**, *358*, 142130. [CrossRef]
11. Khan, H.A.; Naqvi, S.R.; Mehran, M.T.; Khoja, A.H.; Niazi, M.B.K.; Juchelková, D.; Atabani, A. A performance evaluation study of nano-biochar as a potential slow-release nano-fertilizer from wheat straw residue for sustainable agriculture. *Chemosphere* **2021**, *285*, 131382. [CrossRef]
12. Wang, C.; Luo, D.; Zhang, X.; Huang, R.; Cao, Y.; Liu, G.; Zhang, Y.; Wang, H. Biochar-based slow-release of fertilizers for sustainable agriculture: A mini review. *Environ. Sci. Ecotechnol.* **2022**, *10*, 100167. [CrossRef]

13. Wu, W.; Yang, M.; Feng, Q.; McGrouther, K.; Wang, H.; Lu, H.; Chen, Y. Chemical characterization of rice straw-derived biochar for soil amendment. *Biomass Bioenergy* **2012**, *47*, 268–276. [CrossRef]
14. Wang, B.; Ma, Y.; Lee, X.; Wu, P.; Liu, F.; Zhang, X.; Li, L.; Chen, M. Environmental-friendly coal gangue-biochar composites reclaiming phosphate from water as a slow-release fertilizer. *Sci. Total Environ.* **2021**, *758*, 143664. [CrossRef] [PubMed]
15. Kuppusamy, S.; Thavamani, P.; Megharaj, M.; Venkateswarlu, K.; Naidu, R. Agronomic and remedial benefits and risks of applying biochar to soil: Current knowledge and future research directions. *Environ. Int.* **2016**, *87*, 1–12. [CrossRef] [PubMed]
16. ECA. *Restructuring and Planting Vineyards in the EU*; European Court of Auditors: Luxembourg, 2023; p. 51.
17. OIV. State of the World Vine and Wine Sector in 2022. 2023. Available online: https://www.oiv.int/sites/default/files/documents/OIV_State_of_the_world_Vine_and_Wine_sector_in_2022_2.pdf (accessed on 15 January 2025).
18. Dorosh, O.; Rodrigues, F.; Delerue-Matos, C.; Moreira, M.M. Increasing the added value of vine-canes as a sustainable source of phenolic compounds: A review. *Sci. Total Environ.* **2022**, *830*, 154600. [CrossRef]
19. Corcho-Corral, B.; Olivares-Marín, M.; Fernández-González, C.; Gómez-Serrano, V.; Macías-García, A. Preparation and textural characterisation of activated carbon from vine shoots (Vitis vinifera) by H3PO4—Chemical activation. *Appl. Surf. Sci.* **2006**, *252*, 5961–5966. [CrossRef]
20. Li, H.-Y.; Yao, D.-H.; Feng, Q.-J.; Zeng, H.-B.; Liang, J.-M.; Zhou, Z.; Tian, Y.; Zhou, N.; Lu, X.-Y. Adsorption of cd(Ii) and pb(ii) on biochars derived from grape vine shoots. *Desalination Water Treat.* **2018**, *118*, 195–204. [CrossRef]
21. Pinheiro, R.F.; Grimm, A.; Martinello, K.d.B.; Khan, M.R.; Ahmad, N.; Silva, L.F.O.; De Brum, I.A.S.; Dotto, G.L.; dos Reis, G.S. Vine pruning waste-based activated carbon for cerium and lanthanum adsorption from water and real leachate. *J. Rare Earths* **2024**, *42*, 1960–1968. [CrossRef]
22. Manyà, J.J.; González, B.; Azuara, M.; Arner, G. Ultra-microporous adsorbents prepared from vine shoots-derived biochar with high CO_2 uptake and CO_2/N_2 selectivity. *Chem. Eng. J.* **2018**, *345*, 631–639. [CrossRef]
23. Llopart-Roca, P.; Autó, E.; Bayarri, B.; Leardi, R.; Sans, C. Operational parameters affecting synthesis yield and adsorption capacity of vine-pruning derived biochar for pesticide removal: Impact and modelling. *J. Environ. Chem. Eng.* **2025**, *13*, 116005. [CrossRef]
24. Pouretedal, H.R.; Sadegh, N. Effective removal of Amoxicillin, Cephalexin, Tetracycline and Penicillin G from aqueous solutions using activated carbon nanoparticles prepared from vine wood. *J. Water Process Eng.* **2014**, *1*, 64–73. [CrossRef]
25. Deng, W.; Hu, M.; Xu, S.; Hu, M.; Chen, G.; Ji, H.; Zhou, P.; Su, Y. Pyrolysis of sludge briquettes for the preparation of cylindrical-shaped biochar and comparison between CO_2 and steam activation. *Fuel* **2023**, *338*, 127317. [CrossRef]
26. Rawat, S.; Boobalan, T.; Sathish, M.; Hotha, S.; Thallada, B. Utilization of CO_2 activated litchi seed biochar for the fabrication of supercapacitor electrodes. *Biomass Bioenergy* **2023**, *171*, 106747. [CrossRef]
27. Zhang, M.; Gao, B.; Yao, Y.; Xue, Y.; Inyang, M. Synthesis of porous MgO-biochar nanocomposites for removal of phosphate and nitrate from aqueous solutions. *Chem. Eng. J.* **2012**, *210*, 26–32. [CrossRef]
28. Zheng, Y.L.; Wang, B.; Elise, W.A.; Chen, J.J.; He, F.; Chen, H.; Gao, B. Reclaiming phosphorus from secondary treated municipal wastewater with engineered biochar. *Chem. Eng. J.* **2019**, *362*, 460–468. [CrossRef]
29. *ASTM D1762-84*; Standard Test Method for Chemical Analysis of Wood Charcoal. ASTM: West Conshohocken, PA, USA, 2011.
30. Chen, T.; Liu, R.; Scott, N.R. Characterization of energy carriers obtained from the pyrolysis of white ash, switchgrass and corn stover—Biochar, syngas and bio-oil. *Fuel Process. Technol.* **2016**, *142*, 124–134. [CrossRef]
31. Lian, G.; Wang, B.; Lee, X.; Li, L.; Liu, T.; Lyu, W. Enhanced removal of hexavalent chromium by engineered biochar composite fabricated from phosphogypsum and distillers grains. *Sci. Total Environ.* **2019**, *697*, 134119. [CrossRef]
32. Wang, B.; Lehmann, J.; Hanley, K.; Hestrin, R.; Enders, A. Adsorption and desorption of ammonium by maple wood biochar as a function of oxidation and pH. *Chemosphere* **2015**, *138*, 120–126. [CrossRef]
33. Vamvuka, D.; Loupasis, E.; Chamilaki, E.; Sdoukou, E. Adsorption of ammonium from wastewaters by an almond kernel derived biochar modified by potassium hydroxide or dolomite and activated by steam. *Environ. Adv.* **2024**, *15*, 100465. [CrossRef]
34. Enders, A.; Hanley, K.; Whitman, T.; Joseph, S.; Lehmann, J. Characterization of biochars to evaluate recalcitrance and agronomic performance. *Bioresour. Technol.* **2012**, *114*, 644–653. [CrossRef]
35. Li, S.; Galoustian, T.; Trejo, H. Biochar pyrolyzed with concentrated solar radiation for enhanced nitrate adsorption. *J. Anal. Appl. Pyrolysis* **2023**, *174*, 106131. [CrossRef]
36. Zhang, T.; Xu, H.; Li, H.; He, X.; Shi, Y.; Kruse, A. Microwave digestion-assisted HFO/biochar adsorption to recover phosphorus from swine manure. *Sci. Total Environ.* **2018**, *621*, 1512–1526. [CrossRef]
37. Castejón-del Pino, R.; Cayuela, M.L.; Sánchez-García, M.; Sánchez-Monedero, M.A. Nitrogen availability in biochar-based fertilizers depending on activation treatment and nitrogen source. *Waste Manag.* **2023**, *158*, 76–83. [CrossRef]
38. Xie, F.; Wu, F.; Liu, G.; Mu, Y.; Feng, C.; Wang, H.; Giesy, J.P. Removal of Phosphate from Eutrophic Lakes through Adsorption by in Situ Formation of Magnesium Hydroxide from Diatomite. *Environ. Sci. Technol.* **2014**, *48*, 582–590. [CrossRef]
39. Deng, W.; Zhang, D.; Zheng, X.; Ye, X.; Niu, X.; Lin, Z.; Fu, M.; Zhou, S. Adsorption recovery of phosphate from waste streams by Ca/Mg-biochar synthesis from marble waste, calcium-rich sepiolite and bagasse. *J. Clean. Prod.* **2021**, *288*, 125638. [CrossRef]

40. Chen, G.; Wang, Y.; Wang, J.; Wang, J.; Yu, F.; Ma, Q.; Cheng, Z.; Yan, B.; Song, Y.; Cui, X. Production of potassium-enriched biochar from Canna indica: Transformation and release of potassium. *Waste Manag.* **2023**, *164*, 119–126. [CrossRef] [PubMed]
41. Yao, Y.; Gao, B.; Zhang, M.; Inyang, M.; Zimmerman, A.R. Effect of biochar amendment on sorption and leaching of nitrate, ammonium, and phosphate in a sandy soil. *Chemosphere* **2012**, *89*, 1467–1471. [CrossRef] [PubMed]
42. Xu, K.; Lin, F.; Dou, X.; Zheng, M.; Tan, W.; Wang, C. Recovery of ammonium and phosphate from urine as value-added fertilizer using wood waste biochar loaded with magnesium oxides. *J. Clean. Prod.* **2018**, *187*, 205–214. [CrossRef]